NASA Technical Memorandum 84656

ANALYSIS OF AEROTHERMAL LOADS ON SPHERICAL DOME PROTUBERANCES

GEORGE C. OLSEN AND R. E. SMITH

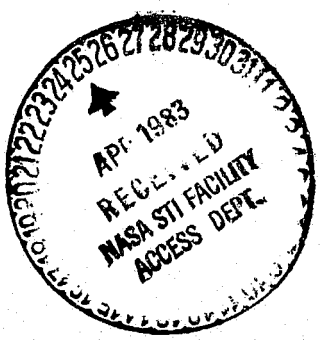

APRIL 1983

National Aeronautics and Space Administration

Langley Research Center
Hampton, Virginia 23665

ANALYSIS OF AEROTHERMAL LOADS ON SPHERICAL DOME PROTUBERANCES

George C. Olsen
R. E. Smith
NASA Langley Research Center
Hampton, Virginia

Abstract

Hypersonic flow over spherical dome protuberances was investigated to determine increased pressure and heating loads to the surface. The configuration was mathematically modeled in a time-dependant three-dimensional analysis of the conservation of mass, momentum (Navier-Stokes), and energy equations. A boundary mapping technique was used to obtain a rectangular parallelepiped computational domain, and a MacCormack explicit time-split predictor-corrector finite difference algorithm was used to obtain solutions. Results show local pressures and heating rates for domes one-half, one, and two boundary layer thicknesses high were increased by factors on the order of 1.4, 2, and 6, respectively. However, because lee-side pressure and thermal loads were reduced the two lower height domes did not experience any net increase in total loads. The total loads on the higher dome were increased by twenty-five percent. Flow over the lower dome was everywhere attached while flow over the intermediate dome had small windward and leeside separations. The higher dome had an unsteady windward separation region and a large leeside separation region. Trailing vortices form on all domes with intensity increasing with dome height. Discussions of applying the results to a thermally bowed thermal protection system are presented.

Nomenclature

c_v	specific heat at constant volume (eq. 5)
e	internal energy
h	dome height above flat plate
K	thermal conductivity of air
k	variable grid concentration parameter (eq. 14)
L_ξ, L_η, L_ζ	differential operators (eq. 19)
P	pressure
R_g	gas constant (eq. 4)
r	radius measured from dome centerline
r_o	radius of flat-plate/dome intersection
T	temperature
t	time
u, v, w	velocity components
$\bar{\gamma}$	functional relationship between the physical and computational domains (eqs. 13 and 15)
x, y, z	coordinate directions
δ_{fp}	flat plate boundary-layer thickness at $x = x_c$
ε	one-half the fillet width
ξ, η, ζ	transformed coordinates
$\bar{\eta}$	redistributed transformed coordinate (eq. 14)
μ	viscosity (eq. 6)
ρ	density
τ_{ij}	stress tensor (eq. 2)

Subscripts

max	maximum coordinate value
c	coordinate value at dome centerline

Introduction

Protuberances in the form of large-diameter small-height spherical domes often occur on hypersonic vehicles as a result of hardware design or thermal bowing. Hypersonic flow over these protuberances can produce increases in local wall pressures and heating rates. Interest in this flow configuration and computation of the pressure and heating rate distributions on them has increased because of proposed alternative metallic Thermal Protection Systems (TPS) to replace the fragile Reusable Surface Insulation (RSI) on the original Space Shuttle.[1,2,3] Titanium and/or superalloy designs that are weight competitive with RSI and offer the advantages of mechanical fastening, longer life, and increased damage resistance have been fabricated.

However, the use of metallic TPS can introduce some physical phenomena not present in the RSI system. One such phenomenon is thermal bowing of the metallic TPS panels.[3] Bowing can occur because metals have relatively large coefficients of thermal expansion and because in the course of performing their function as a thermal protection system the TPS panels must sustain large temperature gradients through their thickness. These conditions lead to large thermal expansion of the outer portion of the panel and small thermal expansion of the inner portion of the panel. The square panels are held down at the corners but otherwise thermal expansion is unrestrained. As a result the center of the panel bows out into the stream so that the vehicle moldline is altered. An array of panels would take on a quilted configuration.

Analytical and experimental studies of two-dimensional flow over a wavy-wall are available in the literature, however, extrapolation of these results to the three-dimensional flow over an array of bowed panels or spherical dome protuberances results in an inaccurate description of the phenomena. The analysis must be done in three-dimensions to adequately predict the physical flows. No analytical studies of a configuration resembling the thermally bowed TPS were found in the literature, probably because large amounts of computer time and storage are required to perform the analysis. Consequently, this preliminary study was undertaken to determine if the increased pressure and heating effects were significant and

if the problem required in-depth consideration. Thermally bowed panels were modeled by the generic configuration of spherical domes. Numerical gridding and computer storage limitations prohibited modeling an array of full scale TPS panels so a single row of 4.6 inch diameter domes was selected to be compatible with the gridding requirements. Dome heights of 0.1, 0.2, and 0.4 inches were considered in a flow field with a laminar-boundary-layer thickness of 0.2 inches. Free stream conditions are for Mach 7 flight at 120,000 ft. altitude. The analysis of this flow configuration will yield dimensionally similar solutions. However, the proper balancing of the similarity parameters to ascertain that the small scale processes in the boundary layer will fall into the similarity pattern requires additional analytical and experimental data not yet available.[4] Therefore, no extension of the results of this study to larger protuberances will be made at this time.

The analysis employs a three-dimensional formulation of the time dependent equations for conservation of mass, momentum, and energy. A MacCormack explicit time-split predictor-corrector finite difference algorithm was used to obtain a steady-state solution on Langley's Cyber 203 vector processing computer. The results of those solutions are presented in this paper using state-of-the-art computer graphics techniques.

A comprehensive experimental program to verify the results obtained in this analysis is scheduled for a later time. Some preliminary small scale tests have provided qualitative correlation with some of the predicted phenomena; no experimental data will be presented in this paper.

Analysis

Governing Equations

Aerothermal loads on spherical domed protuberances were computed by mathematically modeling the flow field with the continuum mechanics equations of motion. Air, the fluid medium, was modeled as a compressible, viscous, thermally conducting gas. Limiting assumptions include considering air as an isotropic, newtonian ideal gas in local thermodynamic equilibrium. The three-dimensional time-dependant system of equations describing this model include the continuity equation (conservation of mass), the Navier-Stokes equations of motion (conservation of momentum), the energy equation (conservation of energy), and the ideal gas equation (thermodynamic state equation). These equations have been derived in the literature[5] and are shown below written in cartesian tensor form where repeated indices indicate a summation over the range of indices (i.e., $\frac{\partial(\rho w_i)}{\partial X_i}$ for i = 1, 2, 3 is $\frac{\partial \rho w_1}{\partial X_1} + \frac{\partial \rho w_2}{\partial X_2} + \frac{\partial \rho w_3}{\partial X_3}$). In addition w_1, w_2, w_3 are the velocity components u, v, w, and X_1, X_2, X_3 are the coordinate directions x, y, z. The Kronecker delta, δ_{ij}; equals 1 when i = j and equals zero when i ≠ j.

Continuity equation,

$$\frac{\partial \rho}{\partial t} + \frac{\partial(\rho w_i)}{\partial X_i} = 0 \qquad \text{for } i = 1, 2, 3 \qquad (1)$$

Navier-Stokes equations of motion,

$$\frac{\partial(\rho w_i)}{\partial t} + \frac{\partial(\rho w_i w_j)}{\partial X_j} + \frac{\partial(\tau_{ij})}{\partial X_j} = 0$$

where

$$\tau_{ij} = \delta_{ij} P - \mu\left(\frac{\partial w_i}{\partial X_j} - \frac{\partial w_j}{\partial X_i} - \frac{2}{3}\delta_{ij}\frac{\partial w_k}{\partial X_k}\right) \qquad (2)$$

for i, j, k = 1, 2, 3

(results in three equations, one for each coordinate direction)

Energy equation,

$$\frac{\partial(\rho e)}{\partial t} + \frac{\partial(\rho e w_j)}{\partial X_j} - K\frac{\partial T}{\partial X_j} + \frac{\partial(w_i \tau_{ij})}{\partial X_j} = 0 \qquad (3)$$

for i, j, k, = 1, 2, 3

Ideal gas state equation,

$$P = \rho R_g T \qquad (4)$$

These equations along with the ideal gas relationship,

$$e = c_v T \qquad (5)$$

and the Sutherland viscosity formula,

$$\mu = 2.270\ \frac{T^{3/2}}{T + 198.6} \times 10^{-8}\ \frac{\text{lb sec}}{\text{ft}^2} \qquad (6)$$

constitute a set of five partial differential equations and one algebraic equation in six dependant variables: three velocity components, u, v, and w; density, ρ; temperature, T; and pressure, P.

The physical domain of the problem is shown in figure 1. The thermally bowed TPS is modeled as a series of domes on a flat plate. Because of symmetry planes at the center of each dome and between domes, only one-half of a dome need be modeled. The dome was specified by its height, h, above the flat plate and its radius, r_o, at the dome/flat plate intersection. The intersection between the dome and flat plate was made mathematically smooth by modeling a fillet region at $r_o \pm \varepsilon$ with a Hermite polynomial.

Boundary Conditions

A boundary layer profile was input as the upstream boundary plane data and held constant throughout the computations. The boundary layer profile was determined using a two-dimensional

boundary layer analysis[6] for flow over a flat plate. The flow configuration is shown in figure 1 and free stream conditions for Mach 7 flight at an altitude of 120,000 ft. are listed in Table I. The boundary layer profiles for the starting plane are shown in figure 2. These profiles, along with a crossflow velocity, w, of zero were impressed on the starting plane (x = 0) and held constant throughout the computations. For a flat plate with no dome the boundary layer height, δ_{fp}, at the center of the three-dimensional region ($x = x_c$) is 0.2 inches. Dome heights, h, with ratios h/δ_{fp} = 0.5, 1, and 2 were investigated. The ratio of dome radius to boundary layer height, r_o/δ_{fp}, was held constant at 11.5.

Both side boundaries are planes of symmetry on which the dependent variables are determined by quadratic extrapolation from interior points so that the cross flow gradients, $\partial/\partial z$, of all state variables are zero and the cross flow velocity, w, is zero. The upper boundary and downstream boundaries are specified as no change boundaries, i.e., set equal to the plane next to them. The flat-plate/dome surface is a no-slip boundary with a constant wall temperature of 1440°R. This wall temperature is both the upper use temperature and the flat plate radiation equilibrium temperature for the input boundary conditions for a titanium TPS assuming a high emittance coating and zero thermal diffusivity.

Computational Domain

In order to generate a boundary fitted coordinate system and provide increased resolution in the boundary layer, the physical domain (fig. 1) was transformed into a rectangular parallelepiped computational domain using a two-boundary grid generation technique.[7] The computational domain, shown in figure 3, has equally spaced grid lines in the ξ, η, and ζ directions.

Transformation of the governing differential equations, eqs. 1, 2, and 3, to the computational domain requires replacement of all spatial derivatives, $\partial/\partial X_i$ for i = 1, 2, 3, with the following,

$$\frac{\partial}{\partial X_i} = \frac{\partial}{\partial C_\ell}\frac{\partial C_\ell}{\partial X_i} \tag{7}$$

where C_ℓ for ℓ = 1, 2, 3 are the transformed coordinates ξ, η and ζ, i.e.,

$\frac{\partial}{\partial X_i} = \frac{\partial}{\partial \xi}\frac{\partial \xi}{\partial X_i} + \frac{\partial}{\partial \eta}\frac{\partial \eta}{\partial X_i} + \frac{\partial}{\partial \zeta}\frac{\partial \zeta}{\partial X_i}$. The resulting equations of motion are,

Continuity,

$$\frac{\partial \rho}{\partial t} + \frac{\partial(\rho w_i)}{\partial C_\ell}\frac{\partial C_\ell}{\partial X_i} = 0 \tag{8}$$

Navier Stokes equations of motion

$$\frac{\partial(\rho w_i)}{\partial t} + \frac{\partial(\rho w_i w_j)}{\partial C_\ell}\frac{\partial C_\ell}{\partial X_j} + \frac{\partial(\tau_{ij})}{\partial C_\ell}\frac{\partial C_\ell}{\partial X_j} = 0 \tag{9}$$

where

$$\tau_{ij} = \delta_{ij} P - \mu\left(\frac{\partial w_i}{\partial C_m}\frac{\partial C_m}{\partial X_j} + \frac{\partial w_j}{\partial C_m}\frac{\partial C_m}{\partial X_i} - \frac{2}{3}\delta_{ij}\frac{\partial w_k}{\partial C_m}\frac{\partial C_m}{\partial X_k}\right)$$

Energy Equation

$$\frac{\partial(\rho e)}{\partial t} + \frac{\partial}{\partial C_\ell}\left(\rho e w_j - K\frac{\partial T}{\partial C_m}\frac{\partial C_m}{\partial X_j}\right)\frac{\partial C_\ell}{\partial X_j} + \frac{\partial(w_i \tau_{ij})}{\partial C_\ell}\frac{\partial C_\ell}{\partial X_j} = 0 \tag{10}$$

Written in short form the system of partial differential equations is,

$$\frac{\partial U}{\partial t} + \frac{\partial F}{\partial C_\ell}\frac{\partial C_\ell}{\partial x} + \frac{\partial G}{\partial C_\ell}\frac{\partial C_\ell}{\partial y} + \frac{\partial H}{\partial C_\ell}\frac{\partial C_\ell}{\partial z} = 0 \tag{11}$$

where,

$$U = \begin{bmatrix} \rho \\ \rho u \\ \rho v \\ \rho w \\ \rho e \end{bmatrix}$$

$$F = \begin{bmatrix} \rho u \\ \rho uu - \tau_{11} \\ \rho uv - \tau_{12} \\ \rho uw - \tau_{13} \\ \rho eu - K\frac{\partial T}{\partial C_m}\frac{\partial C_m}{\partial x} - (u\tau_{11} + v\tau_{12} + w\tau_{13}) \end{bmatrix}$$

$$G = \begin{bmatrix} \rho v \\ \rho uv - \tau_{12} \\ \rho vv - \tau_{22} \\ \rho vw - \tau_{32} \\ \rho ev - K\frac{\partial T}{\partial C_m}\frac{\partial C_m}{\partial y} - (u\tau_{12} + v\tau_{22} + w\tau_{32}) \end{bmatrix}$$

$$H = \begin{bmatrix} \rho w \\ \rho uw - \tau_{13} \\ \rho vw - \tau_{23} \\ \rho ww - \tau_{33} \\ \rho ew - K\frac{\partial T}{\partial C_m}\frac{\partial C_m}{\partial z} - (u\tau_{13} + v\tau_{23} + w\tau_{33}) \end{bmatrix}$$

The required Jacobian transform matrix,

$$J = \left[\frac{\partial C_l}{\partial X_j}\right] = \begin{bmatrix} \frac{\partial \xi}{\partial x} & \frac{\partial \xi}{\partial y} & \frac{\partial \xi}{\partial z} \\ \frac{\partial \eta}{\partial x} & \frac{\partial \eta}{\partial y} & \frac{\partial \eta}{\partial z} \\ \frac{\partial \zeta}{\partial x} & \frac{\partial \zeta}{\partial y} & \frac{\partial \zeta}{\partial z} \end{bmatrix} \tag{12}$$

is determined by a linear mapping of the boundaries at η= 0 and η= 1 of the computation domain onto the boundaries of the physical domain at y = 0 and $y = y_{max}$ in the following form;

$$\bar{Y} = \bar{Y}\ (\xi, 1, \zeta)\ \eta + \bar{Y}\ (\xi, 0, \zeta)\ (1 - \eta). \tag{13}$$

Further transformation to increase resolution in the boundary layer region entails an exponential grid stretching in the η direction of the form,

$$\bar{\eta} = \frac{e^{k\eta}-1}{e^{k}-1} \tag{14}$$

where k is a free parameter that adjusts grid spacing. Equation 13 becomes,

$$\bar{Y} = \bar{Y}(\xi, 1, \zeta)\,\bar{\eta} + \bar{Y}(\xi, 0, \zeta)\,(1-\bar{\eta}) \tag{15}$$

For the geometry of the subject problem the resulting Jacobian matrix is of the form,

$$J = \begin{bmatrix} \frac{1}{x_{max}} & 0 & 0 \\ \frac{\partial \eta}{\partial x} & \frac{\partial \eta}{\partial y} & \frac{\partial \eta}{\partial z} \\ 0 & 0 & \frac{1}{z_{max}} \end{bmatrix} \tag{16}$$

where $\frac{\partial \eta}{\partial x}$, $\frac{\partial \eta}{\partial y}$, and $\frac{\partial \eta}{\partial z}$, which vary for the flat plate, fillet, and dome regions as defined by the radius measured from the dome centerline,

$$r = \sqrt{(x_{max}\,\xi - x_c)^2 + (z_{max}\,\zeta)^2} \tag{17}$$

are shown in the Appendix.

These Jacobian elements are calculated and stored for each grid point in the domain thus allowing the solutions from the computational domain to be transformed to the physical domain.

Substituting the transform Jacobian (eq. 16) into the short form of the equation system (eq. 11) reduces the system to the following,

$$\frac{\partial U}{\partial t} + \frac{\partial F}{\partial \xi}\frac{1}{x_{max}} + \frac{\partial F}{\partial \eta}\frac{\partial \eta}{\partial x} + \frac{\partial G}{\partial \eta}\frac{\partial \eta}{\partial y} + \frac{\partial H}{\partial \eta}\frac{\partial \eta}{\partial z} + \frac{\partial H}{\partial \zeta}\frac{1}{z_{max}} = 0 \tag{18}$$

Numerical Procedure

A finite-difference solution to the governing equations was attained using the second-order accurate MacCormack explicit time-split predictor-corrector algorithm.[8] The algorithm splits the differencing scheme into a series of one-dimensional operators. The operator in the principle flow direction, L_ξ, advances the computation by one time increment while the operators in the other two coordinate directions, L_η and L_ζ, are divided into two steps of one-half a time-increment each and applied symmetrically around the principle flow direction operator. This arrangement allows the principle flow direction operator to run at a Courant, Friedricks, Lewy (CFL) number close to the optimum value of one. The operators are applied serially as follows:

$$U^{n+1}_{i,j,k} = \left[L_\eta\left(\frac{\Delta t}{2}\right)\right]\left[L_\zeta\left(\frac{\Delta t}{2}\right)\right]\left[L_\xi(\Delta t)\right]\left[L_\zeta\left(\frac{\Delta t}{2}\right)\right]\left[L_\eta\left(\frac{\Delta t}{2}\right)\right]\left(U^{n}_{i,j,k}\right) \tag{19}$$

Each operator has two steps, a predictor step that advances the solution by its time increment based on a backward spatial differencing of the one-dimensional equations and a corrector step that recalculates the advancement based on a forward spatial differencing of the predicted results and averages the result with the predictor. The predictor must therefore lag the corrector by a spatial increment in each coordinate direction. The combination of these two steps results in a second-order-accurate differencing scheme in time and space. As an example the first operation $L_\eta(\Delta t/2)$ applied to the data at time step n is as follows,

Predictor step:

$$\bar{U}_{i,j,k} = U^{n}_{i,j,k} - \frac{\frac{\Delta t}{2}}{\Delta \eta}\left[\left(F^{n}_{j} - F^{n}_{j-1}\right)\frac{\partial \eta}{\partial x} + \left(G^{n}_{j} - G^{n}_{j-1}\right)\frac{\partial \eta}{\partial y} + \left(H^{n}_{j} - H^{n}_{j-1}\right)\frac{\partial \eta}{\partial z}\right]_{i,k} \tag{20}$$

Corrector step:

$$\bar{U}^{*n+1}_{i,j,k} = \frac{1}{2}\left(\bar{U}_{i,j,k} + U^{n}_{i,j,k} - \frac{\frac{\Delta t}{2}}{\Delta \eta}\left[\left(\bar{F}_{j+1} - \bar{F}_{j}\right)\frac{\partial \eta}{\partial x} + \left(\bar{G}_{j+1} - \bar{G}_{j}\right)\frac{\partial \eta}{\partial y} + \left(\bar{H}_{j+1} - \bar{H}_{j}\right)\frac{\partial \eta}{\partial z}\right]\right)_{i,k} \tag{21}$$

Where bars over the variables indicate predictor values and asterisks over the variables indicate an intermediate result in the serial application of operators as shown in equation 19. The other operators have similar form.

Although a complete stability analysis of this algorithm is not available the CFL limit yields a conservative time step as follows,

$$\Delta t \le \min\left[\frac{|u|}{\Delta x} + \frac{|v|}{\Delta y} + \frac{|w|}{\Delta z} + c\sqrt{\frac{1}{\Delta x^2} + \frac{1}{\Delta y^2} + \frac{1}{\Delta z^2}}\right]^{-1} \tag{22}$$

where c is the local speed of sound.

In the formulation of this algorithm terms of order three and higher have been truncated. These terms are not significant in many flow regimes, but, when modeling high energy flow fields with strong shocks, as in this paper, they can be significant. In the region of a shock, where

Multiple pages missing from available version

(Pages 4 thru 13)